

Mapping the Yellow River Delta land subsidence with multitemporal SAR interferometry by exploiting both persistent and distributed scatterers

Bowen Zhang^{a,b}, Robert Wang^{a,b,*}, Yunkai Deng^{a,b}, Peifeng Ma^{c,d}, Hui Lin^d, Jili Wang^{a,b}

^a Department of Space Microwave Remote Sensing System, the Institute of Electronics, Chinese Academy of Sciences, Beijing, China

^b University of Chinese Academy of Sciences, Beijing 100049, China

^c Key Laboratory of Urban Land Resources Monitoring and Simulation, Ministry of Land and Resources, Shenzhen 518034, China

^d Institute of Space and Earth Information Science, The Chinese University of Hong Kong, Hong Kong, China



ARTICLE INFO

Keywords:

Persistent scatterers
Distributed scatterers
Yellow River Delta
Sentinel-1
ENVISAT ASAR

ABSTRACT

Due to highly compressible soil and a large amount of human activity, the costal deltas are more prone to ground subsidence. Many major costal deltas in the world are facing subsidence and are consequently more susceptible to flooding, salinization and seawater infusion or even permanent submergence. Therefore, ground subsidence has been a significant problem in coastal delta areas worldwide. The Yellow River Delta (YRD) is the second largest river delta in China. On the one hand, the YRD contains a large area of wetlands rich in biodiversity, and on the other hand, industrial activities and urbanization are extensive due to abundant underground resources such as oil, gas and brine. Excessive land use has caused different degrees of ground subsidence in this area. However, a detailed and comprehensive description of the ground subsidence pattern over the YRD has not been provided. Also, widespread non-urban area in Yellow River Delta region, such as wetlands, farmland and coastal tidal areas, hinders the application of persistent scatterer interferometry method (PSI) for comprehensive subsidence measurement over the whole area. In this paper, we developed a multitemporal InSAR method to map ground subsidence over the YRD area by exploiting both persistent scatterers (PS) and distributed scatterers (DS). This method is characterized by employing the coherence-weighted phase-linking algorithm for fast and reliable optimal phase reconstruction of each DS point and a two-tier network of PS and DS for the robust analysis of land subsidence. To extract the detailed and comprehensive ground subsidence over the whole YRD, we apply our method to 30 ENVISAT ASAR images (2007–2010) and 49 Sentinel-1A (S-1A) images (2015–2018) and obtain measurements of the ground subsidence during these two periods. Forty-one Sentinel-1B (S-1B) images (2016–2018) are also exploited for cross-sensor consistency validation with the result derived from the S-1A dataset. Our method shows a great advantage over the PSI method, providing much higher measuring point (MP) density in mapping land subsidence over the YRD, including 15-fold higher density for the ASAR dataset, 5.1-fold for the S-1A dataset and 5.3-fold for the S-1B dataset, which enables a very detailed description of local ground deformation patterns. Cross-track consistency in the derived measurements from the S-1A and S-1B datasets shows a standard deviation of 9.6 mm/yr for the vertical subsidence rate. A quantitative validation of the derived subsidence results compared with leveling measurements suggests an accuracy of 4.58 mm/yr for the standard deviation term. By comparing the ground deformation over the YRD during the periods of 2015–2018 and 2007–2010, we find that the subsidence in this region shows an overall intensification trend and many new and severe subsidence depressions appear along the coastline, with a maximum vertical subsidence rate of 432 mm/yr. Subsequently, the overextraction of underground brine for salt production is identified as the primary factor causing the ground subsidence near the YRD coastal area.

1. Introduction

A delta is a low-lying plain that is naturally formed when rivers flow into the sea or other bodies of water. Globally, deltas are one of the most densely populated areas in the world, with more than 300 million

people worldwide living on or near coastal delta regions (Syvitski et al., 2009). However, because of the highly compressible soils and large amount of human activity, ground subsidence has been a significant problem for many deltas in the world (Chaussard et al., 2013; Törnqvist et al., 2008). Land subsidence may lead coastal delta areas to be more

* Corresponding author.

E-mail address: yuwang@mail.ie.ac.cn (R. Wang).

vulnerable to coastal flooding, saltwater intrusion and infrastructure instability (Nicholls and Cazenave, 2010). Therefore, detailed and accurate ground subsidence measurements are crucial for reducing natural hazards and economic losses over coastal deltaic regions.

The Yellow River Delta (YRD) is in the northern Shandong Province, China and is the location where the Yellow River joins the sea. The YRD spans an area of over 10,000 km² and supports more than 6 million people. On the one hand, YRD contains large wetlands with a rich biodiversity, which are habitats for hundreds of animals and plant species, as well as resting places for migratory birds. On the other hand, the YRD is an important industrial zone in China for oil and gas exploration, salt production, aquaculture, etc. The abundant resources have contributed to rapid economic development in recent years; however, uncontrolled overexploitation of underground resources and increasing human activities have caused serious ground subsidence in the YRD.

However, until now, a comprehensive and detailed ground subsidence measurement over the whole YRD area was not obtained. Although in situ observation techniques such as leveling (Liu and Huang, 2013) and sediment borehole measurements (Zhang et al., 2018) have been employed, the low spatial-temporal resolution of these techniques limits their application for large-scale monitoring. Synthetic aperture radar interferometry (InSAR) is an ideal alternative to investigate the magnitude, distribution and temporal changes in ground subsidence over the YRD due to the broad coverage, high special resolution, and all-weather operational ability (Bamler and Hartl, 1998). However, the conventional InSAR technique is limited by temporal decorrelations and atmospheric artifacts (Zebker and Villasenor, 1992). Multitemporal InSAR (MT-InSAR) techniques exploit datasets spanning long time intervals and focus on coherent radar targets to extend the applicability of InSAR (Ferretti et al., 2001; Berardino et al., 2002). Persistent scatterer interferometry (PSI) and distributed scatterer interferometry (DSI) are two main categories of MT-InSAR.

PSI exploits a single-master strategy to produce interferograms by co-registering all images to a common master image (Ferretti et al., 2001). In addition, PSI focuses on only point-like radar targets exhibiting high intensity and stable phase characteristics over all observation periods, most of which are artificial objects such as building facades and corners (Cresotto et al., 2016). This limitation of PSI results in few measurement points (MPs) in coastal delta areas, such as the YRD area, which is characterized by widespread natural wetlands, tidal flats and other low-reflectivity regions.

Recently, some researchers, like Zhu and Bamler (2010, 2011) and Ma and Lin (2016), extended the capability of PSI to complex built urban area regarding to overlaying problem by SAR tomography. Especially, in Tomo-PSInSAR (Ma and Lin, 2016), to improve the robustness of estimation, beamforming is utilized together with an M-estimator for parameter estimation in a two-tier network and a ridge estimator is used for network adjustment. However, this method is still an extension of the PSI and encounters difficulty in achieving effective deformation monitoring in rural areas such as the PRD area.

In contrast to PSI, DSI exploits distributed scatterers, which usually contain groups of pixels sharing similar radar returns and usually correspond to bare soil, sparsely vegetated land or highways. In DSI techniques, to minimize the decorrelation, only small spatial/temporal baseline multi-master interferograms are utilized. Typical DSI approaches include SBAS (Berardino et al., 2002; Lanari et al., 2004), StamPS/MTI (Hooper, 2008), and TCPInSAR (Zhang et al., 2011). Some researchers have exploited these methods to study ground subsidence over the YRD. For example, Liu et al. (2015) utilized the SBAS strategy to study the ground subsidence over the Gudao Oilfield region in the YRD. Liu et al. (2016) exploited the StamPS/MTI method to investigate the ground subsidence pattern over the Dongying Oilfield. However, all these studies only focused on some local deformation in the YRD. In addition, although these DS methods could improve the density of MPs over nonurban areas, it is challenging to achieve comprehensive and

detailed ground deformation measurements over large deltaic regions due to the possible error induced by phase unwrapping (Berardino et al., 2002).

Ferretti et al. (2011) proposed a new-generation MT-InSAR method named SqueeSAR™, which further increases the density of measurement points in rural areas by exploiting both PS and DS information. Specifically, this method uses all $N(N - 1)/2$ wrapped interferograms to obtain the N optimal phase of each DS point, ignoring the limitation of spatial and temporal baselines and avoid the phase unwrapping operation. The DS phase optimization is achieved through the combination of adaptive statistically homogeneous pixel (SHP) identification and optimal phase reconstruction by phase triangulation algorithm (PTA). Extended methods have been proposed, such as CAESAR (Fornaro et al., 2015), PD-PSInSAR (Cao et al., 2016) and CSI (Dong et al., 2018).

Accurate SHP identification is the basis for DS phase reconstruction. Usually, SHP identification is achieved via a two-sample goodness-of-fit test on the amplitude information of pixels. The test process generally only considers the statistic information and ignores the spatial information, which may lead to misclustering of inhomogeneous pixels in the complex environment of surface textures. In SqueeSAR™, the PTA is based on a maximum likelihood (ML) estimation, which is a naturally nonlinear optimization problem and is solved by a quasi-Newton method: Broyden-Fletcher-Goldfarb-Shanno (BFGS). There are two drawbacks of this procedure. First, the covariance matrix inversion operation in the ML estimation may introduce error and reduce estimation performance (Bernstein, 2005). Second, the matrix inversion and BFGS algorithm are both high computational operations (Liu and Nocedal, 1989). These two drawbacks significantly limit the practical applications of these methods for ground subsidence measurements over large areas. For pre-processed DS points, the geophysical parameters are estimated together with PS candidates using the same time series analysis procedure. As the signal quality of DS usually cannot match that of PS, the robust parameter estimation of DS is important.

In this paper, to obtain comprehensive and detailed ground subsidence measurements over the entire YRD, we exploit both PS and DS information through a two-tier network strategy. Considering the robustness of the PS parameter estimation of Tomo-PSInSAR, this paper develops an extension of Tomo-PSInSAR for deformation measurement over nonurban areas. In our method, SHP identification utilizes not only the statistical information but also the spatial information. For DS point phase optimization, a modified estimation model together with a coherence-weighted phase-linking method is implemented for fast and reliable DS preprocessing. Furthermore, for reliable parameter estimation of DS points, we adopt a two-tier network strategy: the most reliable PS points are selected in the first-tier network using a robust parameter estimation procedure (Ma and Lin, 2016), and the DS and remaining PS are selected and solved in the second-tier network based on the result of the first-tier network. Our method is applied to multi-track SAR datasets, including ENVISAT ASAR (2007–2010), Sentinel-1A (2015–2018) and Sentinel-1B (2016–2018), to obtain the ground subsidence of the whole YRD.

To demonstrate the advantages of our method, a comparison among the results of our method and Tomo-PSInSAR for three datasets is carried out. Cross-sensor consistency is evaluated by comparing the deformation rate maps obtained from S-1A and S-1B datasets. Then, leveling data are used to quantitatively validate the derived ground subsidence result from the ENVISAT ASAR dataset. Finally, the spatial-temporal changes in ground subsidence over the YRD between the two periods of 2007–2010 and 2015–2018 are analyzed, and the possible causes for these deformations over the YRD are determined.

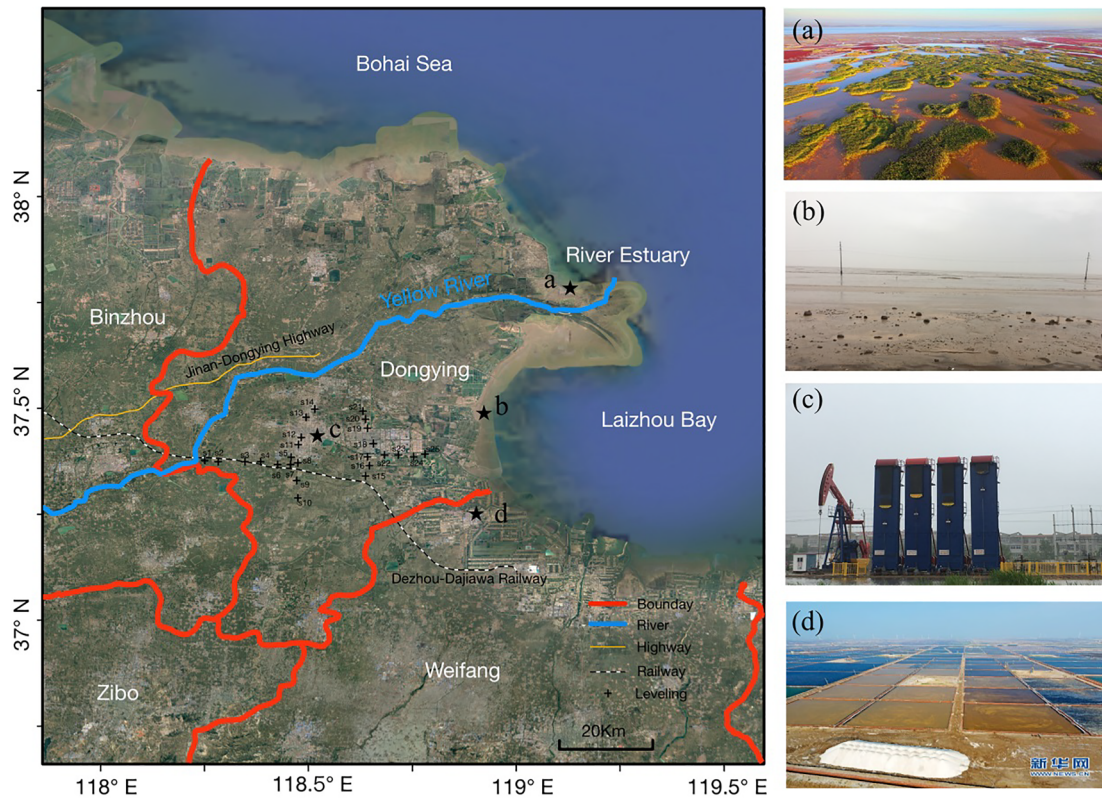


Fig. 1. The Google optical map and geolocation of the study area. (a) A wetland image near the Yellow River estuary, (b) a photo of a coastal tidal flat, (c) an oil extraction machine in Dongying, and (d) an online image of the salt field (Xinhua Net 2016).

2. Study area and datasets

2.1. Study area

The YRD, located between Laizhou Bay and the Bohai Gulf on the northeast coast of China, has gradually formed since the mouth of the Yellow River shifted from the Yellow Sea to the Bohai Sea in 1855 (Shi and Zhang, 2003). Until now, more than 50 channel adjustments have occurred, forming China's second largest estuary delta (Chu et al., 2006). The geolocation of the study area is shown in Fig. 1. Rich water resources and a warm, temperate continental monsoon climate make the Yellow River Delta the only intact, typical and youngest wetland ecosystem in the warm temperate zone in the world with a wetland coverage area of approximately 4500 km². The wild wetlands and tidal flats are shown in Fig. 1(a) and (b).

Hydrocarbon resources are abundant in the YRD. Geologically, the YRD is situated in the Dongying depression, which is a petroliferous Cenozoic basin of the Bohai basin (Zhang et al., 2004). Since the last century, hydrocarbon exploitation has been continuous in the YRD, which has gradually become China's second largest oilfield, the Shengli Oilfield. Fig. 1(c) shows an oil extraction machine in Dongying. In addition, the underground brine resources are rich in this area. Salt fields (Fig. 1(d)) are spread along the entire coastline, and underground brine extraction is the main salt production method for these salt fields. In addition, due to the abundant natural resources and pleasant climate, human activities in this area are becoming increasingly frequent. Heavy land use has made land subsidence in the YRD apparent since the last decade.

2.2. Dataset used

To map the land subsidence in the YRD, the following data are utilized: 30 C-band descending track ENVISAT ASAR data acquired

from path 132 between February 2007 and September 2010, 49 C-band ascending track S-1A data acquired from path 69 between July 2015 and February 2018 and 41 descending track S-1B data acquired from path 76 between October 2016 and February 2018. The detailed information of these three datasets is given in Table 1, and the data coverages are shown in Fig. 2. Fig. 3 shows the temporal and spatial perpendicular baseline distributions of the three datasets. The red mark in each figure indicates the master image for each dataset. The horizontal axis is the acquisition time for each image, and the vertical axis is the perpendicular baseline relative to the master image.

External DEM data acquired from Shuttle Radar Topography Mission with a spatial resolution of 90 m were used to simulate and remove the topographic phase. In particular, due to the large Doppler centroid variation of the Sentinel-1 Terrain Observation by Progressive Scans (TOPS) mode data, highly stringent coregistration is required. Here, an external DEM is used for a geometrical alignment to achieve the TOPS data coregistration (Yagüe-Martínez et al., 2016).

3. Methodology

In this paper, to efficiently obtain a comprehensive and detailed deformation map over a large coastal delta region, we exploit both PS and DS information through a two-tier network strategy. The method consists of three parts: the most reliable PS point selection in the first-

Table 1

Image number and acquisition temporal coverage of the SAR data used in our study.

SAR sensor	Temporal coverage	SLC number	Orbit direction
ENVISAT ASAR	2007-02-01 ~ 2010-09-25	30	Descending
Sentinel-1A	2015-07-01 ~ 2018-02-15	49	Ascending
Sentinel-1B	2016-10-05 ~ 2018-02-21	41	Descending

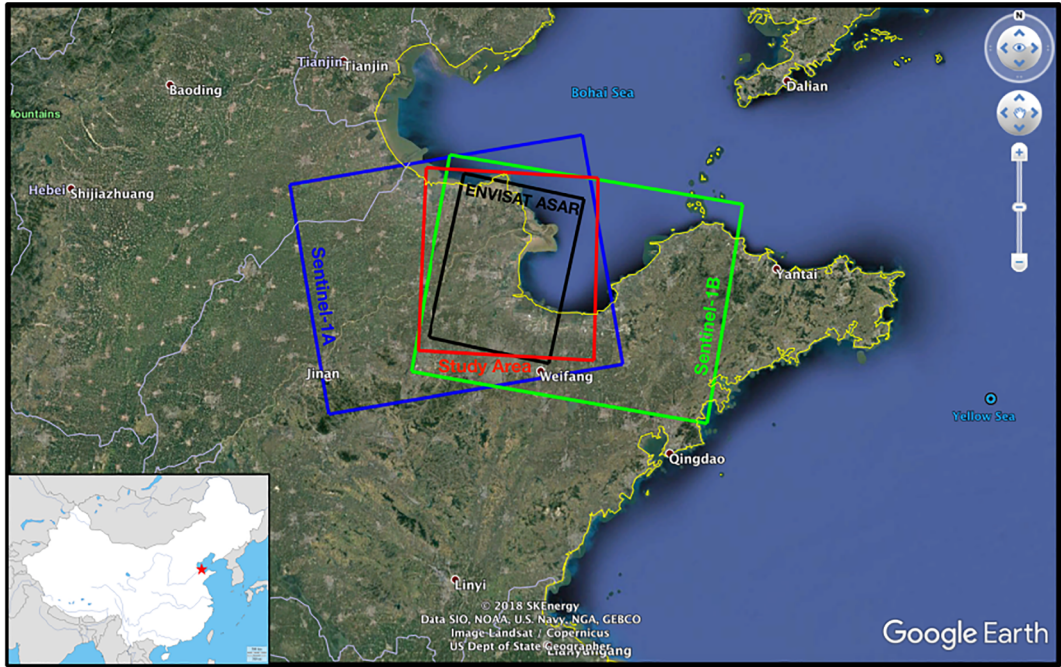


Fig. 2. The image coverages of the ENVISAT ASAR, Sentinel-1A and Sentinel-1B datasets and the study area.

tier network, DS preprocessing, and parameter estimation for the remaining PS and DS points in the second-tier network. The flowchart of the proposed method is shown in Fig. 4.

In the first-tier network, we select the most reliable PS points and obtain their credible geophysical parameters. These points will be used as a reference for parameter estimation of the second-tier network. The DS preprocessing is aimed at fast and reliable optimal phase reconstruction for each DS point. Then, the parameters of DS and the remaining PS candidates are estimated in the second-tier networks. In the following section, detailed explanations of each step are given.

3.1. The most reliable PS point detection in the first-tier network

In the first step, the most reliable PS points are detected in the first-tier network. We select the initial PS candidates (IPSC) based on a stringent amplitude dispersion threshold and high coherence value to ensure that the selected IPSC is most likely true PS points. A Delaunay triangulation is applied to connect these selected points. We treat this triangulation network as the first-tier network.

To guarantee the parameter estimation quality, a robust estimation procedure that combines beamforming with an M-estimator (Huber, 1964; Ma and Lin, 2016) is exploited to estimate the relative

parameters, height and linear motion rate at each arc of the first-tier network. For a given pixel containing one or more targets, the complex signal y_i of i th acquisition can be represented as two dimensional Fourier transform of the reflectivity profile $\gamma(s, v)$ along height s and linear velocity v :

$$y_i = \int_{\Delta s} \int_{\Delta v} \gamma(s, v) \exp\{-j2\pi(\xi_i s + \eta_i v)\} ds dv + n \quad (1)$$

where $\gamma(s, v)$ is the reflectivity profile of all the ground scatters within one resolution cell, $\xi_i = 2B_i/\lambda R$ is determined by spatial baseline B and slant range distance R , $\eta_i = 2t_i/\lambda$, t_i is time baseline, n is the noise term. Δs and Δv are the searching range of the residual height and linear deformation rate. To estimate the parameters s and v , beamforming spectral estimator is adopted here to reconstruct the reflectivity profile:

$$\hat{\gamma}(s, v) = \frac{|\alpha(s, v)^H y|}{\|\alpha(s, v)\|_2 \|\beta\|_2} \quad (2)$$

where $\alpha(s, v) = [\exp(j2\pi(\xi_1 s + \eta_1 v)), \dots, \exp(j2\pi(\xi_N s + \eta_N v))]^T$ is the steering vector, $(\cdot)^H$ is the transpose and conjugate operation, $\|\cdot\|_2$ is the Euclidean norm of a vector. The arcs with $\max(\hat{\gamma}) > T_{PS}$ are reserved, where T_{PS} is user defined threshold value between 0 and 1. In this work, T_{PS} is set to be 0.72. By locating the maximum of $\hat{\gamma}$, we get all the

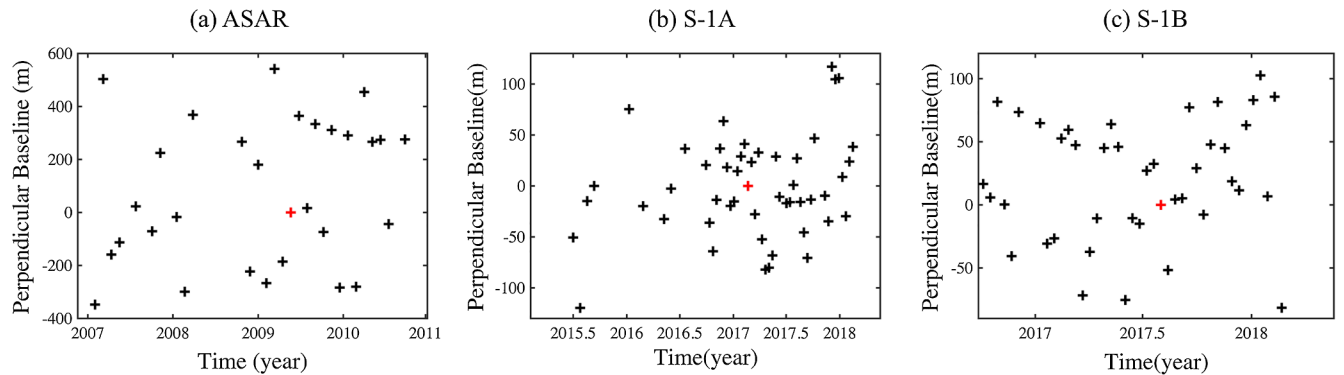


Fig. 3. Baseline configuration of the three datasets used in this study. The red cross represents the master image. (a) ASAR, (b) S-1A and (c) S-1B. (For interpretation of the references to colour in this figure legend, the reader is referred to the web version of this article.)

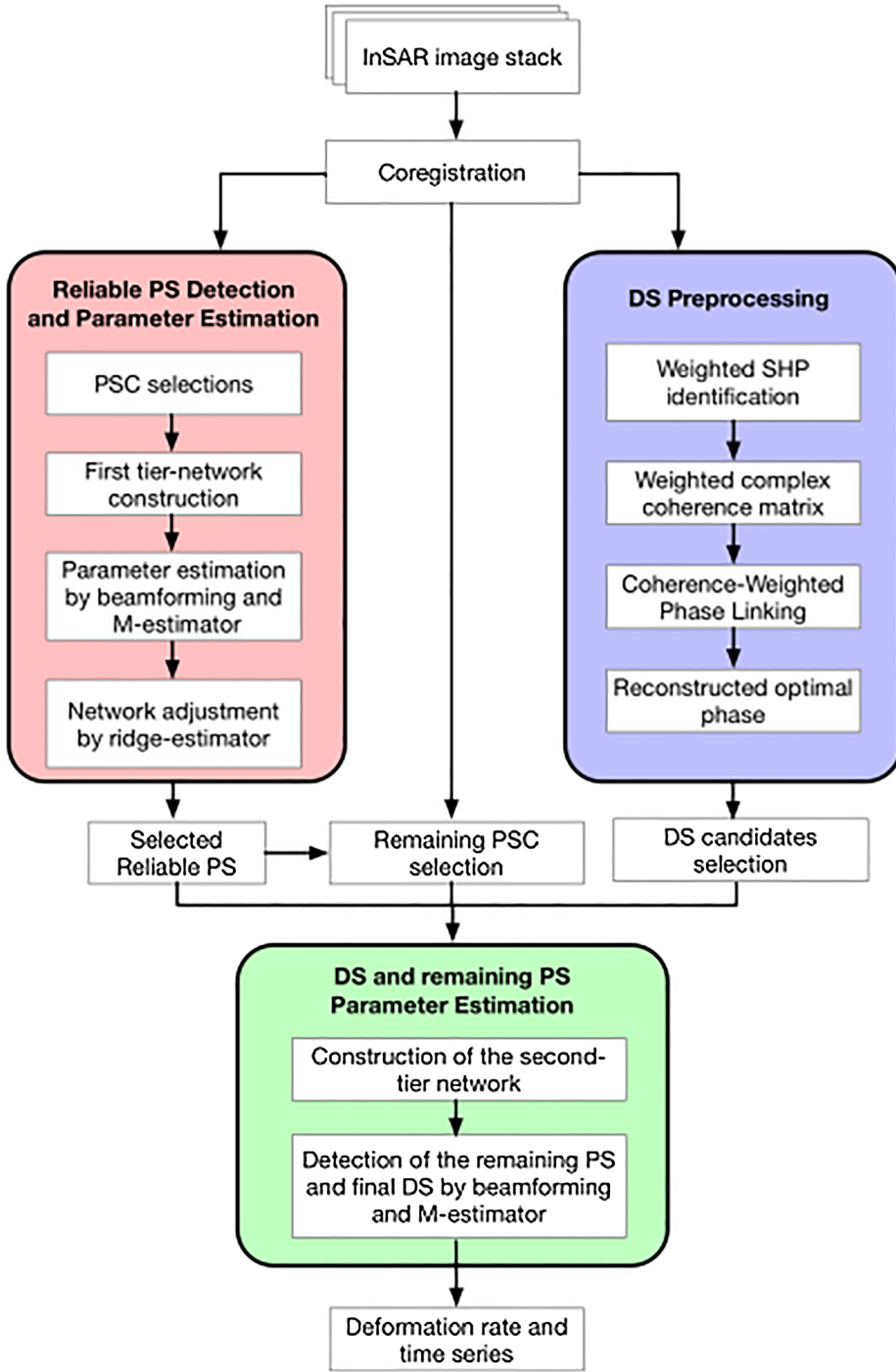


Fig. 4. Flowchart of the proposed algorithm.

relative parameters of v and s on the reserved arcs. But the beamforming method has two drawbacks: it adopts a discrete interval to find the optimal solution in the searching space; it utilizes all SAR observations including those with lower SNR which may degrade the precision of estimation. To further improve the accuracy of parameter estimation in the first-tier network, we combine beamforming with an M-estimator. Temporal phase unwrapping is first conducted based on the preliminary estimates, and then the estimation problem is transformed to a continuous inversion:

$$\Delta\phi = DJ = \begin{bmatrix} 2\pi\xi_1 & 2\pi\eta_1 \\ \vdots & \vdots \\ 2\pi\xi_N & 2\pi\eta_N \end{bmatrix} \begin{bmatrix} s \\ v \end{bmatrix} \quad (3)$$

where $\Delta\phi$ is unwrapping phase. Therefore, the parameters J can be re-estimated in a continuous searching space. To lower the influence of possible unwrapping phase outliers, M-estimator is adopted for final parameter estimation (Ma and Lin, 2016). By iteratively assigning smaller weights to larger residual phases, M-estimator is less vulnerable to phase outliers.

$$\hat{J}^{(t)} = (D^T W^{(t)} D)^{-1} D^T W^{(t)} \Delta\phi \quad (4)$$

where t is the iterate index, W is the dialog weight matrix and its initial is identical matrix. Each element of $W^{(t+1)} = \text{diag}(w_i^{t+1})$ is calculated using the residual phase $r_i^{(t)} = \Delta\phi - D\hat{J}^{(t)}$:

$$W^{(t)} = \begin{cases} 1, & |r_i^{(t)}| < C \\ \frac{C}{|r_i^{(t)}|}, & |r_i^{(t)}| > C \end{cases} \quad (5)$$

where C is set to be 1.345. By combining beamforming and M-estimator, the estimated parameters in the first-tier network are expected to be more robust and reliable.

After obtaining the relative parameters, the absolute parameters of each IPSC with respect to one reference point in the whole area are estimated by integrating the relative parameter through network adjustment. Isolated small networks may appear due to the rejection operation in the last step. As disconnected networks cannot be adjusted together, we identify the largest connected network. The network adjustment problem can be formulated as follows:

$$H = GX \quad (6)$$

where H contains the estimated relative parameters at the arcs; G is the adjustment matrix consisting of -1 , 0 , and 1 , where 1 represents the end PS of the arc and -1 represents the start PS of the arc; and X contains the absolute parameters of the identified PSs. In practice, as the adjustment matrix G may be ill conditioned, small changes in the estimated relative parameters H can cause large changes in the solution X , which means that the inversion is not stable. A ridge estimator is utilized to avoid the possibly ill-adjusted regulatory problem.

$$X = (G^T W G + \sigma I)^{-1} G W H \quad (7)$$

where W is a diagonal weighting matrix that contains the maximum of $\hat{\gamma}$ of each arc to represent the quality of each estimation. The regulation parameter σ can migrate the condition of the adjustment matrix and enable a direct numerical solution. The optimal value of σ can be determined by the L-curve method (Ma and Lin, 2016; Hansen and O'Leary, 1993). In the following steps, the most reliable PS points detected are utilized as references for the other PS and DS point selections and parameter estimations in the second-tier network.

3.2. DS preprocessing

3.2.1. SHP identification

The first step of DS preprocessing is to evaluate the homogeneous similarity of the surroundings with central patches to identify SHPs for each pixel. Many goodness-of-fit statistical hypothesis tests have been applied for homogeneity evaluation. These tests generally only consider the statistical information and ignore the spatial information. In this paper, we introduce an SHP identification method taking both statistical and spatial information into account.

Inspired by the KS test, the statistical distance is set as the max value of the absolute difference between the cumulative distribution functions of two pixels. Precisely, for N coregistered SAR images, the empirical distribution function P_N can be estimated without bias by the sorted amplitude list ($x = |y|$):

$$P_N(X) = \begin{cases} 0 & \text{for } X < x_i \\ i/N & \text{for } x_i \leq X < x_{i+1} \\ 1 & \text{for } X \geq x_N \end{cases} \quad (8)$$

The statistical distance $\Delta(x_1, x_2)$ of the two pixels measures the max value of the absolute difference of empirical distribution functions of the two pixels under investigation, x_1 and x_2 :

$$\Delta(x_1, x_2) = \sqrt{N/2} \sup_x (P_N^{x_1}(x) - P_N^{x_2}(x)) \quad (8)$$

The smaller the value $\Delta(x_1, x_2)$ is, the more similar the two pixels are. We also assume that the closer the spatial distance of two pixels is, the more similar the two pixels are. Therefore, we consider the 2D-

spatial distance $d(x_1, x_2)$ between the two pixels. To effectively reduce the phase noise and preserve the detailed spatial information, we place more weights on similar SHPs. Therefore, a kernel function is used to transform the two distance types to a weight:

$$w(x_1, x_2) = \exp \left(- \left(\frac{d(x_1, x_2)}{\gamma_d} \right)^2 - \left(\frac{\Delta(x_1, x_2)}{\gamma_\Delta} \right)^2 \right) \quad (9)$$

where γ_d and γ_Δ are user-defined scaling factors. γ_d is usually set to 1.443 times the length of the search radius. For γ_Δ , we borrow the idea of the KS test the hypothesis that two sample vectors are drawn from the same distribution if $\Delta(x_1, x_2)$ is smaller than the threshold value c at a fixed significance level α (0.05 in this work). In our experiment, we set γ_Δ as 1.443 c .

For pixel x' in a fixed window centered on pixel x , pixels with high weights (e.g., 0.5) are kept as SHPs of x with corresponding weight $w(x, x')$. Therefore, a weighted average estimator is used to estimate the complex coherence matrix (CCM) using normalized complex scattering vectors $Z(x')$ and the weight $w(x, x')$ of the SHP set Ω :

$$C(x) = \frac{\sum_{x' \in \Omega} w(x, x') Z(x) Z(x')^\dagger}{\sum_{x' \in \Omega} w(x, x')} = |C| \circ \Psi \quad (10)$$

where C is the estimated weighted CCM, Ψ is an $N \times N$ matrix with element $\exp(j\varphi_{ij})$ indicating the interferometric phases between the m th acquisition and n th acquisition, and \circ is a pixel wise production operation.

3.2.2. Optimal phase reconstruction using coherence-weighted phase-linking

After SHP identification and weighted CCM estimation, the next step is reconstruction of the optimal phase $\theta = [\theta_1, \theta_2, \dots, \theta_N]^T$ based on the CCM. The optimal phase reconstruction is under the assumption that the normalized SAR data vector $y \in C^N$ follows a complex multivariate normal distribution. The probability density function is as follows:

$$f(y) = \frac{1}{\pi^N \det(S)} \exp(-y^H S^{-1} y) \quad (11)$$

where S is an $N \times N$ true CCM. Under the assumption that all pixels belonging to Ω can be described by the same phase value θ , the ML estimation of the optimal phase θ can be represented as follows (Cao et al., 2015):

$$\theta = \underset{\theta}{\operatorname{argmax}} \{ \Lambda^H (-|S|^{-1} \circ C) \Lambda \} \quad (12)$$

where $\Lambda = [e^{j\theta_1}, e^{j\theta_2} \dots e^{j\theta_N}]$. Without loss of generality, the first value of θ is set to zero. Therefore, $N - 1$ phase values need to be estimated from the $N(N - 1)/2$ interferogram. In practice, as the true coherence matrix $|S|$ is not accessible, the matrix is substituted by its estimation: $|C|$. As C is a Hermitian matrix, the optimization problem can be converted to the following expression (Cao et al., 2015):

$$\begin{aligned} \theta &= \underset{\theta}{\operatorname{argmax}} \{ \sum ((-|C|^{-1} \circ |C|) \circ \Psi \circ (\Lambda \Lambda^H)^T) \} \\ &= \underset{\theta}{\operatorname{argmax}} \left\{ \sum_{m=1}^N \sum_{n>m}^N \rho_{m,n} \cos(\varphi_{m,n} - \theta_{m,n}) \right\} \end{aligned} \quad (13)$$

where $\theta_{m,n} = \theta_m - \theta_n$, $\rho_{m,n}$ is the element of $-|C|^{-1} \circ |C|$ at row m and column n . In principle, the optimal phase reconstruction process is actually to find the maximum summation of $\cos(\varphi_{m,n} - \theta_{m,n})$ with the corresponding weight term $-|C|^{-1} \circ |C|$.

SqueeSAR™ adopts an iterative optimization algorithm BFGS to solve the ML estimation problem (13) and this algorithm is called a PTA. There are two limitations of this procedure: first, the ML estimation requires the inversion of $|C|$, which is usually not positive and definite if the SHP number is less than the SLC amount, which is more common if the data stack is large. The inversion process may introduce error for the estimation and lead to performance degradation.

Moreover, the BFGS method is extremely time consuming, and the matrix inversion operation is also a time-consuming operation. Because coherence is the direct evaluation standard of the interferogram phase quality, the coherence matrix $|C|$ can be used as the weight, and the matrix inversion operation is effectively avoided. Thus, the optimization question of (13) is converted to the following coherence-weighted form (Cao et al., 2015):

$$\theta_{coh} = \operatorname{argmax}_{\theta} \{ \Lambda^H (|C| \circ \Psi) \Lambda \} = \operatorname{argmax}_{\theta} \{ \Lambda^H C \Lambda \} \quad (14)$$

By assigning a larger weight to the interferometric phase with higher coherence and by avoiding the matrix inversion operation, the estimated phase is expected to be more robust and resistant to decorrelation.

Instead of adopting BFGS for the nonlinear system (14), we borrow the phase-linking method of (Guarnieri and Tebaldini, 2008), which employs an alternating direction technique for the optimal phase reconstruction:

$$\hat{\theta}_n^k = \arg \left\{ \sum_{m \neq n}^N C_{m,n} \exp \left(j \hat{\phi}_m^{k-1} \right) \right\} \quad (15)$$

where k is the iteration step. Compared with BFGS, each iterative step in this method is accomplished with no need for matrix inversion or gradient computation. We call this procedure coherence-weighted phase-linking (CWPL). Then, the quality of the reconstructed optimal phases is measured by the phase quality indicator (Ferretti et al., 2011):

$$\Gamma = \frac{2}{N(N-1)} \operatorname{Re} \left(\sum_{n=1}^N \sum_{m>n}^N e^{j\varphi_{m,n}} e^{-j(\theta_m - \theta_n)} \right) \quad (16)$$

where $\varphi_{m,n}$ is the corresponding phase value in the coherence matrix at row m and col n , and θ_m and θ_n are the reconstructed optimal phases. Γ will be further used for DS candidate selection. Only those DS points with Γ values greater than a user-defined value are reserved as the input for the parameter estimation in the second-tier network.

3.3. DS and remaining PS point parameter estimations in the second-tier network

In the first-tier network, the most reliable PS points are selected. These scatters will act as reference points for the second-tier network. The remaining PS candidates are selected with temporal average amplitudes and relaxed coherence values. The selected DS candidates and remaining PS candidates are the input of the second-tier network. Then, we connect each scatterer to its nearest reference PS points detected in the first tier to form multiple local star networks, which we refer to as the second-tier network.

The robust parameter estimation procedure used for the arc parameter estimation in the first tier is also used here for the geophysical parameter extraction of each arc in the second-tier network. We lower the ensemble coherence slightly to determine whether to preserve this arc. The estimated parameters are relative to the first-tier reference PS points. Then, we obtain the final parameters by directly adding the parameters of the reference point. Layover points could also be resolved in this processing framework, as shown in Ma and Lin (2016). Because the YRD is mainly a nonurban area and the layover is not well represented in moderate-resolution data such as the ASAR and S-1 datasets, we do not detect overlaid points in this study. Moreover, one practice problem is that there may be overlapping points between the selected DS candidates and the remaining PS candidates. For each of these points, we first estimate the parameter by treating it as a PS point. If the parameter is a PS point, we preserve the point and delete it from the DS candidate list. Otherwise, we attempt to estimate the parameter by treating it as a DS point. Then, we judge whether to preserve the point. Finally, we obtain the deformation rate and time-series of the

studied area.

4. Results and analysis

To obtain comprehensive and detailed ground subsidence maps over the whole YRD area, we apply our method to ASAR (2007–2010), S-1A (2015–2018) and S-1B (2016–2018) datasets and obtain the deformation results for the two periods of 2007–2010 and 2015–2018. In the following section, the performance of the algorithm is investigated, which includes DS preprocessing and final deformation measurement results over different datasets. To validate the accuracy of the results, cross-sensor consistency is evaluated through a comparison of the results obtained from the S-1A and S-1B datasets, and leveling data is used to quantitatively validate the derived result from the ASAR dataset.

4.1. DS preprocessing

After obtaining reliable PS points in the first-tier network using the procedure described in Section 3.2, DS preprocessing is performed. The DS preprocessing is composed of SHP identification step and a CWPL optimal phase reconstruction procedure, as shown on the right side of Fig. 5. A 21×21 searching window is adopted to achieve SHP identification in this study. Then, the CCM of each point is estimated using selected weighted SHPs. After obtaining the CCM, the optimal phase sequence can be efficiently reconstructed using the CWPL method as described in Section 3.2.2.

To illustrate the filter performance and computational efficiency of the CWPL method, we select a subset image (5000×2000 R/A) from S-1A datasets with 49 SLCs over the Yellow River mouth area and process the image with a C++ program on a PC with a 2.6 GHz i7 processor. Fig. 5(a) shows the averaged intensity map, and Fig. 5(b) shows the original noisy interferogram corresponding to the data pair with a 145-day temporal baseline. Fig. 5(c) and (d) compare the reconstructed interferograms using PTA and CWPL, respectively. As shown in Fig. 5, both reconstruction methods efficiently filtered the decorrelation phase noise to some extent and preserved the detailed spatial information. Moreover, compared with the PTA method, the CWPL method demonstrates a better performance in phase filtering. For the computational time, the PTA method requires 63 min, but the CWPL only requires 9 min. This demonstrates that the CWPL significantly shortens the time required for the optimal phase reconstruction procedure.

Then, the phase quality indicator Γ of the reconstructed optimal phase is calculated using (16) and is utilized for DS candidate seeding. The selected DS and other remaining PS candidates are utilized in the second-tier network to estimate the final deformation results.

4.2. Deformation rate maps over the YRD

To obtain comprehensive and detailed ground subsidence maps over the whole YRD, we apply our method to ASAR and S-1A datasets, and we obtain the deformation results of two periods: 2007–2010 and 2015–2018. The results are shown in Fig. 6. To validate the accuracy of the results, we also apply our method to the S-1B dataset for cross evaluation of the ground subsidence obtained from the S-1A dataset, which will be shown in Section 4.3. In our experiments, the observed deformation in the line of the sight direction is projected in the vertical direction. As explained in Section 5, the YRD subsidence is mainly caused by the extraction of underground resources, and the deformation caused by this factor is mainly in the vertical direction. To validate the performance of the proposed method, we compare the deformation results extracted using our method and Tomo-PSInSAR for all three datasets. Fig. 6 shows a comparison of the estimated vertical deformation rate maps for three SAR image datasets: ASAR descending track, S-1A ascending track, and S-1B descending track. The ground deformation results are superimposed on the optical images. The left

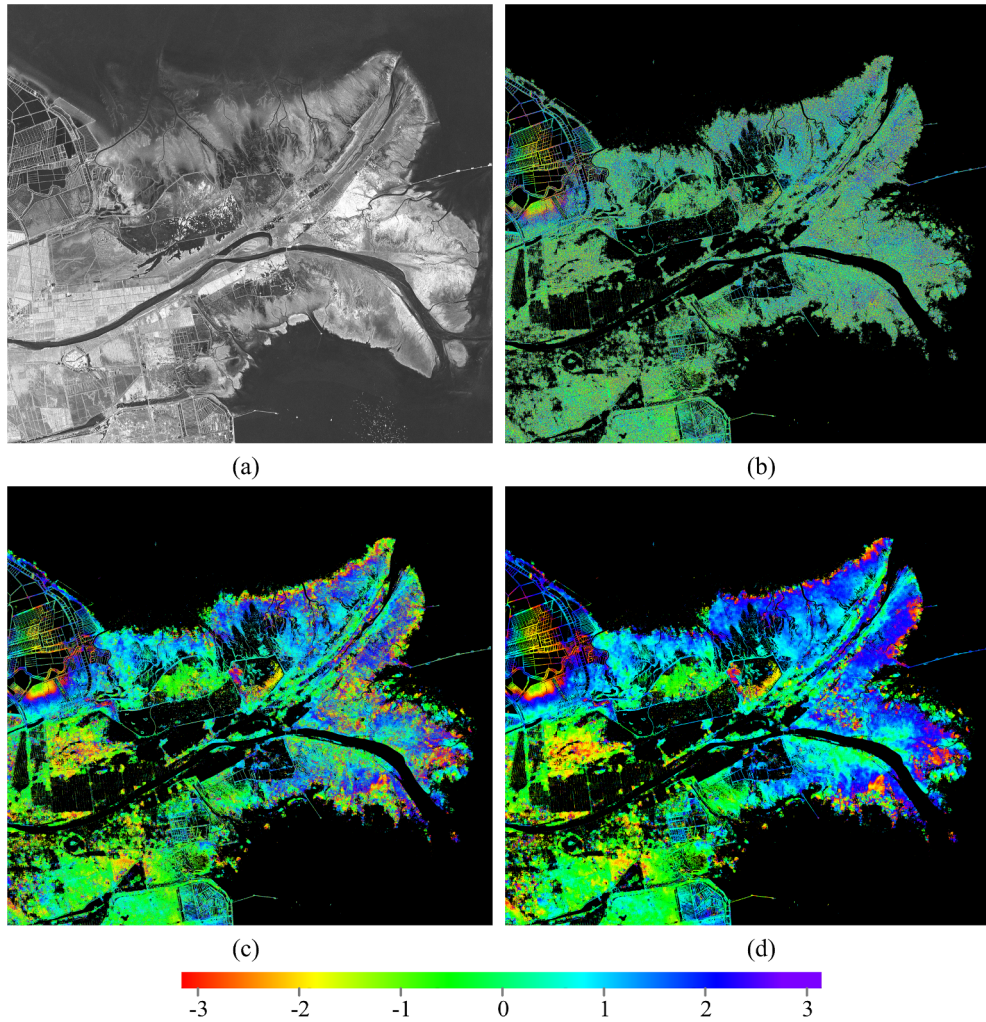


Fig. 5. (a) Temporally averaged amplitude image, (b) original interferogram phase, (c) reconstructed optimal phase using the PTA method, and (d) reconstructed optimal phase using the CWPL method of an interferogram pair (20160929–20170220) from an S-1A dataset over the Yellow River mouth region.

column gives the results obtained using the Tomo-PSInSAR algorithm, and the right column shows the results obtained using our method. As shown in Fig. 6, the deformation signals extracted using our method are more comprehensive than those estimated with Tomo-PSInSAR. The MPs acquired by the Tomo-PSInSAR method are mainly concentrated in urban areas such as buildings, roads, and field ridges. However, our method obtains not only the reliable deformation signal in urban areas but also many MPs in nonurban areas, such as farmland and coastal tidal areas.

Table 2 lists the statistics of the MPs obtained using the two algorithms for all three datasets. Due to the utilization of DS point information, the proposed algorithm obtains far more MPs than the Tomo-PSInSAR method. For the ASAR dataset, there are 15 times more MPs of our method than of Tomo-PSInSAR. For the S-1A and S-1B datasets, there are 5 times more MPs of the proposed method. In addition, S-1 datasets have more points than ASAR, which might be attributed to the S-1 satellites' short revisit times, making estimation of the deformation results more reliable and more remaining MPs. Overall, our method can obtain more detailed ground subsidence information than Tomo-PSInSAR over different SAR datasets. In the following section, the accuracy of the estimated deformation results is evaluated.

4.3. Accuracy assessment of the deformation measurements

4.3.1. Cross comparison between S-1A ascending track and S-1B descending track derived vertical deformation rates

We verify the cross-sensor consistency of the derived ground deformation rate obtained from the S-1A ascending track and the S-1B descending track. We selected the overlapping period from October 2016 to February 2018 and the overlapping area for comparison. Considering that the geometric positions of the observation points will be different due to the different imaging geometries, we first unified the MPs to the same geometric coordinates. The vertical deformation rate of each grid is calculated by averaging the ground deformation rate of the MPs that falls in the grid. Fig. 7(a) shows the scatter correlation plots of the vertical deformation rates of two SAR datasets, which have a good correlation of 0.95. The root mean square error (RMSE) of the difference is 1.56 mm/yr. The histogram of the deformation rate difference in the two SAR datasets is given in Fig. 7(b). The mean and variance of the deformation rate difference are 0.19 mm/yr and 9.85 mm/yr, respectively. The results were consistent between the ground deformation rate extracted using two datasets. The reason for the difference may be due to the different positions of the scatterers in the same resolution grid between different tracks. As shown in the ground subsidence measurement results, most of the YRD area faces pronounced land subsidence, and the deformation gradient is relatively large. Therefore, the ground subsidence rate of two point with

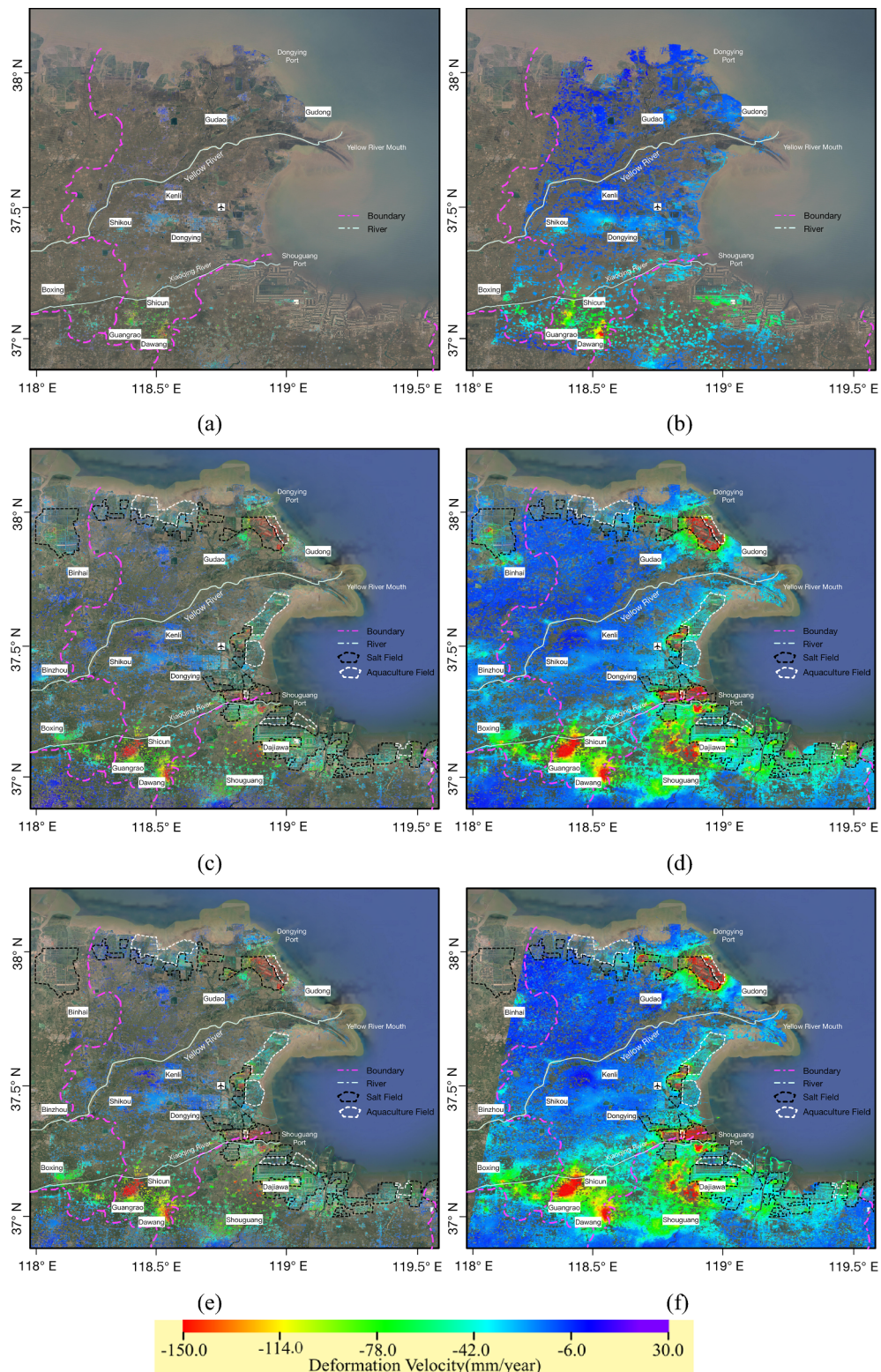


Fig. 6. Vertical deformation rates over the YRD during the period of 2007–2010 obtained from ASAR (top row), 2015–2018 obtained from S-1A (middle row) and 2016–2018 obtained from S-1B (bottom row) datasets using the Tomo-PSInSAR and our method. (a), (c) and (e) Tomo-PSInSAR and (b), (d) and (f) our method. The background image is an optical image of the corresponding area.

relatively close distance may vary greatly.

4.3.2. Validation of the ASAR-derived vertical deformation rates using leveling data

We compared deformation measurement results derived from the

ASAR dataset with 25 second-order leveling measurements acquired by the Lubei Institute of Geological and Prospecting Engineering. Leveling data MPs were obtained during 2007 and 2008 and have a one-year overlap period with the ASAR dataset. The locations of leveling measurements are marked in Fig. 1. To enable the comparison, we use the

Table 2

Number of MPs of the Tomo-PSInSAR and our method for all three datasets.

	Number of MPs	
	Tomo-PSInSAR	Our Method
ENVISAT ASAR	243 181	3 763 181
Sentinel-1A	2 909 048	14 701 558
Sentinel-1B	2 202 586	11 690 959

InSAR-derived MPs in the range of the 100 m * 100 m center with the leveling point to calculate the average annual deformation rate for 2007–2008. The comparison results are shown in Fig. 8. The standard deviation of the deformation rate difference between the two measurements is 4.58 mm/yr, which implies that the InSAR measurement results are highly consistent with the leveling measurement results. The discrepancies between InSAR and leveling-derived results may be attributed to a few causes. One reason is that the InSAR MPs are not exactly matched with the leveling positions. Another factor is that a time span displacement exists between the leveling acquisition data and the InSAR datasets. For these reasons, it is inevitable that there are some differences between the leveling and InSAR-derived average deformation rates.

In summary, good consistency is maintained between different SAR datasets and between InSAR and leveling measurements, which indicates that the proposed algorithm can achieve comprehensive, accurate and reliable surface deformation measurements over the large costal YRD region.

5. Land subsidence characteristics and causal factors analysis

The vertical deformation rate map of Fig. 6 shows that the land subsidence characteristics over the YRD are quite different between the 2007–2010 and 2015–2018 periods. In this section, we first analyze the spatial-temporal changes in surface deformation between the two periods over the YRD. Then, the deformation causes over the YRD are analyzed.

5.1. Spatial-temporal variations in ground subsidence of the YRD and causal analysis

Fig. 6 illustrates the vertical deformation rate map over the YRD region for two time periods: the deformation rate map from February 2007 to September 2010 measured from the ENVISAT ASAR dataset is shown in Fig. 6(b), and the deformation rate map from July 2015 to February 2018 measured from the S1-A dataset is shown in Fig. 6(d).

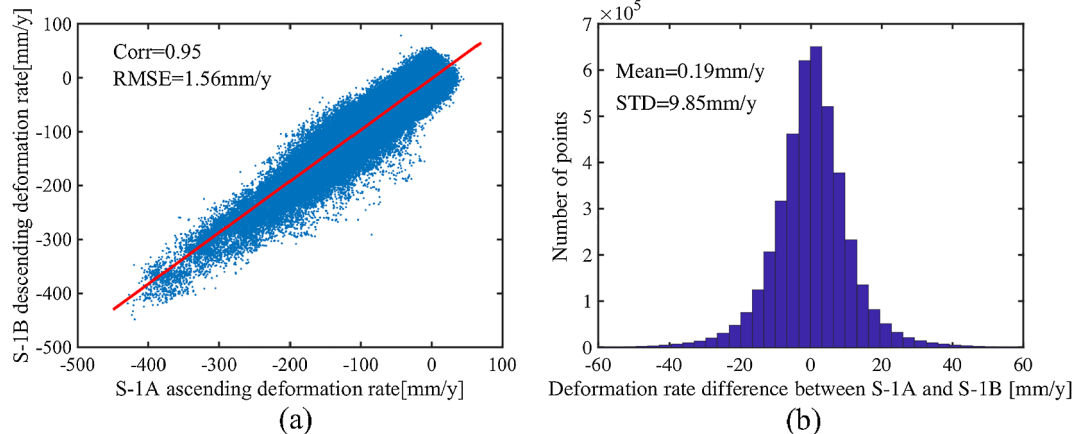


Fig. 7. Cross comparison of the measured vertical deformation of the S-1A and S-1B datasets. (a) Correlation between the linear vertical deformation rate over the common period estimated from the two datasets. (b) Histogram of the vertical deformation rate difference.

The YRD surface deformation characteristics between 2015 and 2018 are quite different from those between 2007 and 2010. Three types of changes are observed: several new subsidence zones appear near the coastline; ground subsidence around Guangrao County is intensified; and ground subsidence in the Dongying Oilfield slows down.

5.1.1. Appearance of new subsidence zones along the coastline

During the period from 2015 to 2018, a new, large ground subsidence zone appeared near the Dongying Port on the northern bank of the Yellow River estuary. The enlarged surface deformation rate maps of this region during the period of 2007 to 2010 and 2015 to 2018 are given in Fig. 9(a) and (b), respectively. During the 2007–2010 period, the ground subsidence rate does not exceed 50 mm/yr in this region. However, a large ground subsidence depression appears during the 2015–2018 period, with a maximum subsidence rate of 432 mm/yr, which is marked as P in Fig. 9. The surface deformation rate profiles of two time periods along the N-S and W-E lines passing through the P point, as marked in Fig. 9, are given in Fig. 10(a) and (b), respectively. The accumulated ground subsidence at the maximum deformation point P during the 2015–2018 period is given in Fig. 12, which illustrates that the largest accumulated subsidence reached 1.15 m within 3 years.

Fig. 9(c) and (d) show optical images over this region in 2007 and 2017. Two main changes are observed in the optical images: many chemical factories are newly built near Dongying Port, and more land was used for salt production. The optical images of the enlarged chemical factories and salt fields, marked as A and B in Fig. 9(d), are shown in Fig. 9(e) and (f), respectively. We can conclude from Fig. 9 that the distribution of the salt field is highly correlated with the distribution of the ground subsidence depression in this region. The appearance of this newly built salt field is closely correlated with the industrial development of Dongying Port. Because industrial salt is one of the basic raw materials for the chemical industry, many salt fields were built nearby. Moreover, the YRD region is rich in underground brine, whose salt concentration is higher than that of seawater. Therefore, the salt production of these salt fields mainly relies on underground brine extraction. Therefore, the overexploitation of brine for salt production and the chemical industry is the main reason for the new subsidence region near Dongying Port.

The newly appeared ground deformation zone along the Laizhou Bay rim is also related to salt production. This area has been a famous salt field since the Song Dynasty. Fig. 11 shows an enlarged ground subsidence map over the coastal zone of Laizhou Bay during the period of 2015–2018. The three large deformation regions of A, B, and C correspond to the Guangrao Salt Field, Yangkou Salt Field, and Yongfeng Salt Field, respectively. Fig. 12 shows the accumulative time-series

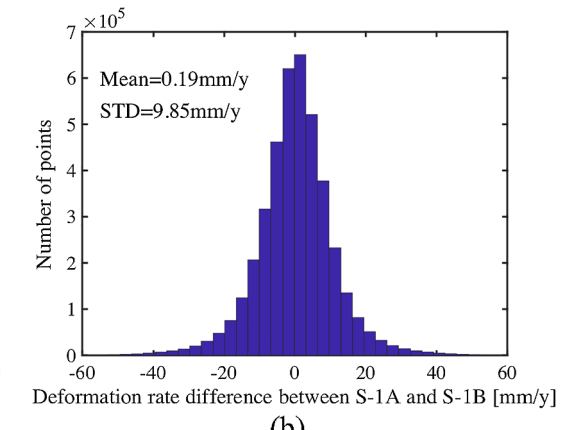


Fig. 8. Comparison of the measured vertical deformation of the ENVISAT ASAR and Sentinel-1 datasets. (a) Correlation between the linear vertical deformation rate over the common period estimated from the two datasets. (b) Histogram of the vertical deformation rate difference.

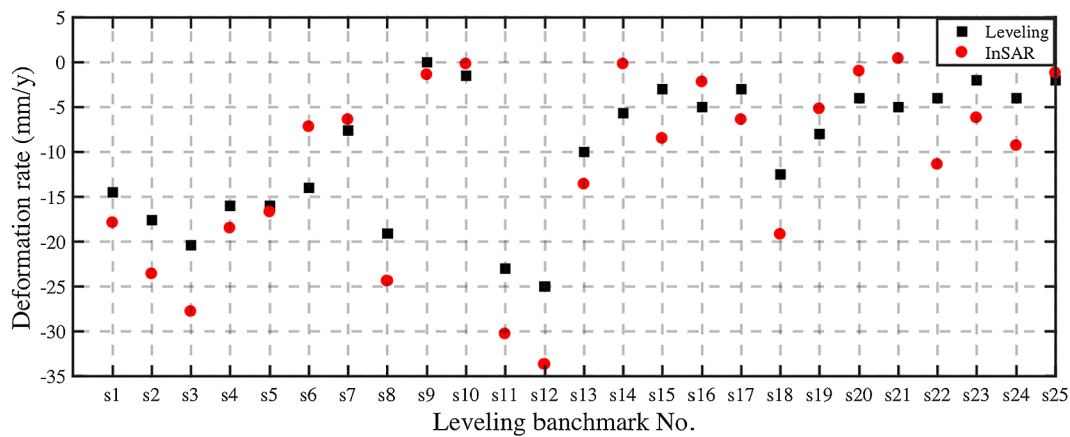


Fig. 8. Comparison between InSAR results and leveling measurements from 2007 to 2008. The locations of the leveling benchmarks of s1-s25 are marked in Fig. 1.

subsidence. The maximum subsidence rate is 330 mm/yr. The time-series shows that the deformation in this area is almost linear with rapid settlement, and the maximum settlement accumulation reached 0.84 m.

In addition, the deformation of Binhai County in the northwestern part of the study area is highly consistent with the distribution of coastal salt fields. From the analysis above, we find that the major and severe surface subsidence along the coast of the YRD is highly correlated with salt production.

5.1.2. Ground subsidence intensification around Guangrao County

Another notable change is that the land subsidence around Guangrao County became more pronounced. The enlarged surface deformation maps during the periods of 2007–2010 and 2015–2018 over Guangrao County are given in Fig. 13(a) and (b), respectively. The ground subsidence of the entire region presents a more pronounced trend, with severely subsided zones expanding outwards. The area covered by the red line in Fig. 13 is the area where the subsidence rate is greater than 100 mm/yr. During the period of 2007–2010, the maximum subsidence rate of 155 mm/yr appeared in Dawang. However, the maximum subsidence location shifted to Shicun during the period of 2015–2018, with the subsidence rate reaching 258 mm/yr. Fig. 14 shows the optical maps of the new built industry zone around Shicun in 2007, 2011 and 2015, which are marked as purple rectangles in Fig. 13. The distribution of newly built factories is closely correlated with the distribution of the ground subsidence extension in this area. Therefore, the expansion of the industrial area, which leads to increased demand for water, can be identified as the predominant factor for the increase in ground subsidence around the Guangrao region. Fig. 15 shows two cracked walls in this region, which illustrate that severe ground subsidence may damage infrastructure.

5.1.3. Slowing of ground subsidence in the Dongying Oilfield

Another severe ground subsidence area that was observed during the period of 2007–2010 is the Dongying-Shikou-Kenli region, located in the central part of the study area, which is a large oil extraction region of the Shengli Oilfield. The enlarged subsidence rate maps over the periods of 2007–2010 and 2015–2018 are given in Fig. 16. We found that the ground subsidence in this area has been slightly relieved in recent years. The accumulated subsidence map of points A and B, marked in Fig. 16, during the two periods are shown in Fig. 17. The subsidence depression in region A gradually disappeared from 2015 to 2018, and the subsidence rate of region B changed from approximately 40 mm/yr to approximately 25 mm/yr. The red dotted line in Fig. 16 indicates the distribution of the oil extraction region, which has a high correlation with the subsidence area. The ground subsidence rate decrease over this area may account for the possible oil extraction reduction in recent years or more sophisticated water flooding methods

used during exploitation to improve recovery capability (Liu et al., 2016).

In general, the surface subsidence in the YRD has shown an overall intensification trend. Several new subsidence depressions appeared along the coastline. The ground subsidence along the Xiaoqing River and its southern region have become more severe, and the rapid deformation region is expanding. The activity of the Dongying-Kenli-Shikou deformation zone has slowed in recent years, but this area still shows a tendency of slow subsidence. In the next section, the possible impact factors for the uneven deformation in the YRD are discussed.

5.2. Causal factors of ground subsidence in the YRD

5.2.1. Salt production

From the surface deformation distribution shown in Fig. 6(d), the distribution of the large deformation zone and the salt fields along the YRD coast is highly consistent. The underground brine resource is abundant in the YRD, and underground brine extraction is the main production method used in coastal salt fields in the YRD.

As discussed in the last section, the formation of the newly appeared large deformation zone along the coastline, such as the Dongying Port region and Laizhou Bay rim zone, shown in Figs. 9 and 11, respectively, is highly correlated with the presence of the salt fields. The newly built chemical factories require a large amount of raw chemical materials such as industrial salt, which led to the construction of new salt fields in the region. The overexploitation of underground brines for salt production may lead to development of the region as the new, most severe subsidence zone in the YRD.

5.2.2. Oil exploitation

The YRD contains China's second largest oilfield, Shengli Oilfield, and oil exploitation has continued since the last century. The reduction of oil will reduce the pressure within the reservoir, causing the reservoir to shrink, which may lead to land surface subsidence. In addition, during oil extraction, it is usually necessary to extract groundwater from surrounding areas for reinjection, which may cause further surface subsidence in the surrounding area.

The Dongying-Kenli-Shikou Oilfield area, shown in Fig. 16, and the Gudao-Gudong Oilfield, shown in Fig. 6, are two important oil extraction areas of the Shengli Oilfield. As discussed in the last section, since 2009, the ground subsidence in the Dongying-Kenli-Shikou Oilfield has been gradually relieved. The ground subsidence over the Gudao-Gudong Oilfield during the period of 2015–2018 did not change much compared with the subsidence over the 2008–2010 period.

5.2.3. Artificial facilities

With economic development and city expansion, many artificial

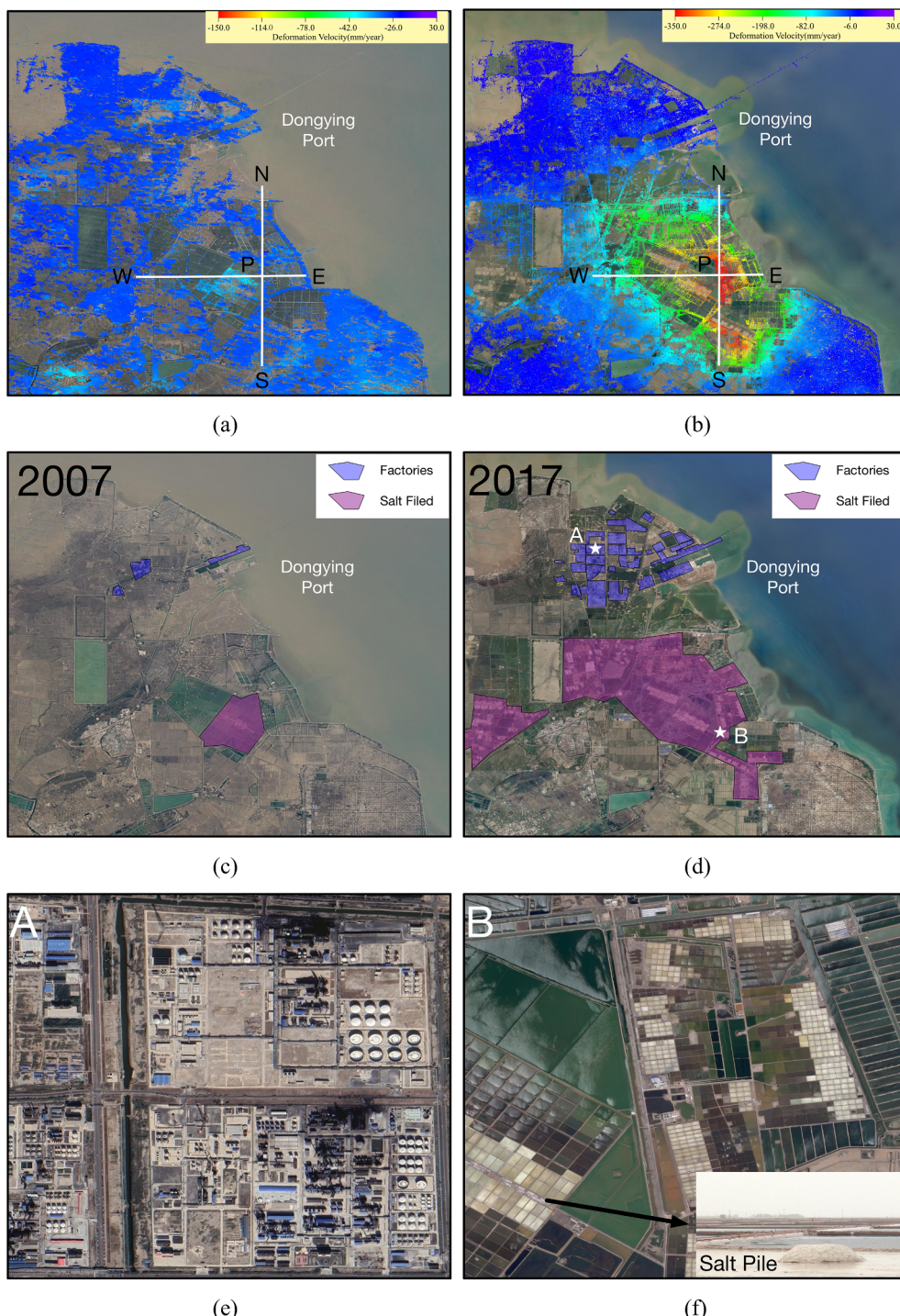


Fig. 9. Vertical subsidence rate map near Dongying Port for the periods of (a) 2007–2010 and (b) 2015–2018. Optical image and the distribution of factories and salt fields near Dongying Port in (c) 2007 and (d) 2017. (e) Enlarged industry map of A. (f) Enlarged salt field map of B.

facilities have been built in the YRD, such as buildings, railways, and highways. These facilities increase the pressure on the ground and cause the soil to compress, leading to the occurrence of local subsidence.

For example, the Jinan-Dongying highway, finished in 2016, and the Dezhou-Dajiawa railway, built in 2015 and shown in Fig. 18, are currently undergoing subsidence. Fig. 18(c) and (d) show ground subsidence profile A-B, which is across the highway, and profile C-D, which is across the railway line. The deformation along the expressway and the railway line is more serious than that in the periphery. These results show that the construction of artificial facilities may also cause local

subsidence in the YRD area.

5.2.4. Aquaculture

As shown in Fig. 6, the high correlation between the distribution of aquaculture fields and the land deformation suggests that aquaculture is also a causal factor for the ground subsidence over the YRD due to its high reliance on groundwater. During winter, the temperature of seawater is low. To keep fish and shrimp safe for the winter, it is necessary to extract groundwater with a higher temperature than seawater. Moreover, shrimp are kept in salty water, but too-high salinity may reduce production. Therefore, farmers often continuously extract

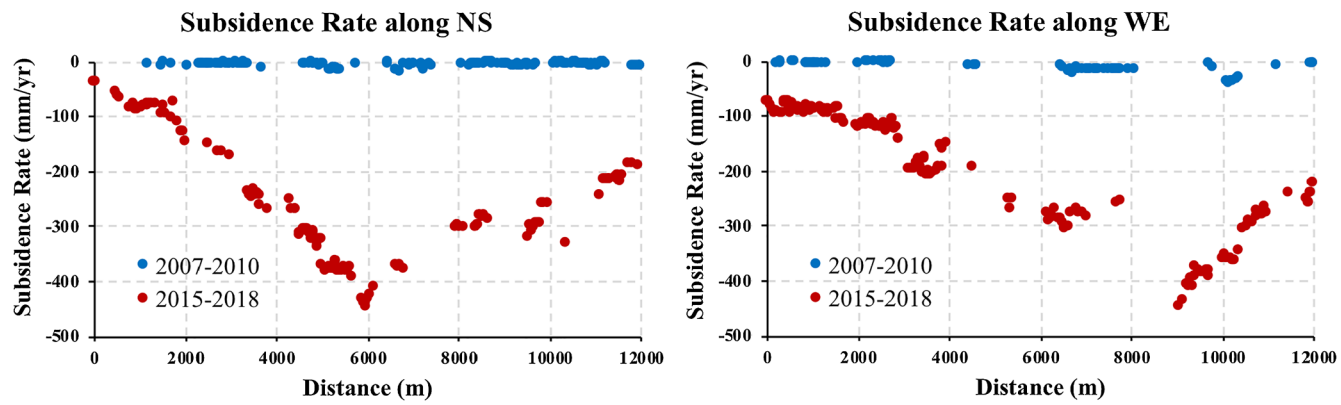


Fig. 10. Vertical subsidence rate profiles along the NS and WE directions marked in Fig. 9.

groundwater to dilute the brackish water in the pond.

5.2.5. Sediment consolidation

The compaction of sediments has always been one of the most important natural factors for surface subsidence in most worldwide delta regions. Sandy and clayey soil are the two main components of sediments in the YRD. However, researchers have shown that the natural consolidation is almost complete; the ground subsidence caused by this factor has decreased to less than 5 mm per year (Shi et al., 2007). Compared with the severe deformation faced by the YRD, this natural factor can be ignored. The uneven ground deformation is mainly caused by human activities.

5.3. Discussion

From the above analysis, we found that the YRD is facing serious surface subsidence and that the subsidence has shown an intensification trend in recent years. The main causes of subsidence are human activities, including excessive exploitation of underground natural resources (underground brine, water, hydrocarbons, etc.) and the increasing number of human facilities. The severe subsidence may threaten human and natural environmental health in the YRD in many

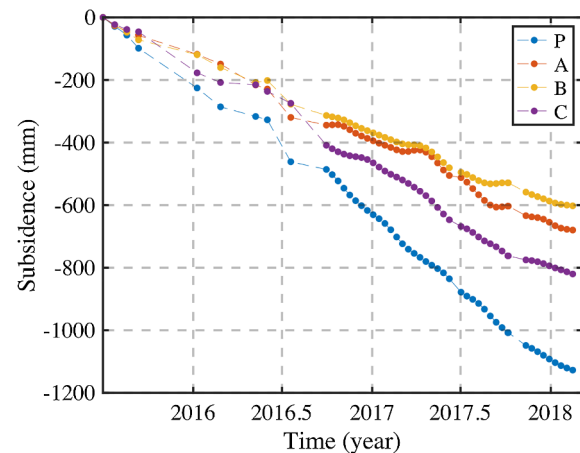


Fig. 12. Accumulated subsidence at point P with the maximum subsidence rate marked in Fig. 8 and points A, B, C, which are marked in Fig. 11.

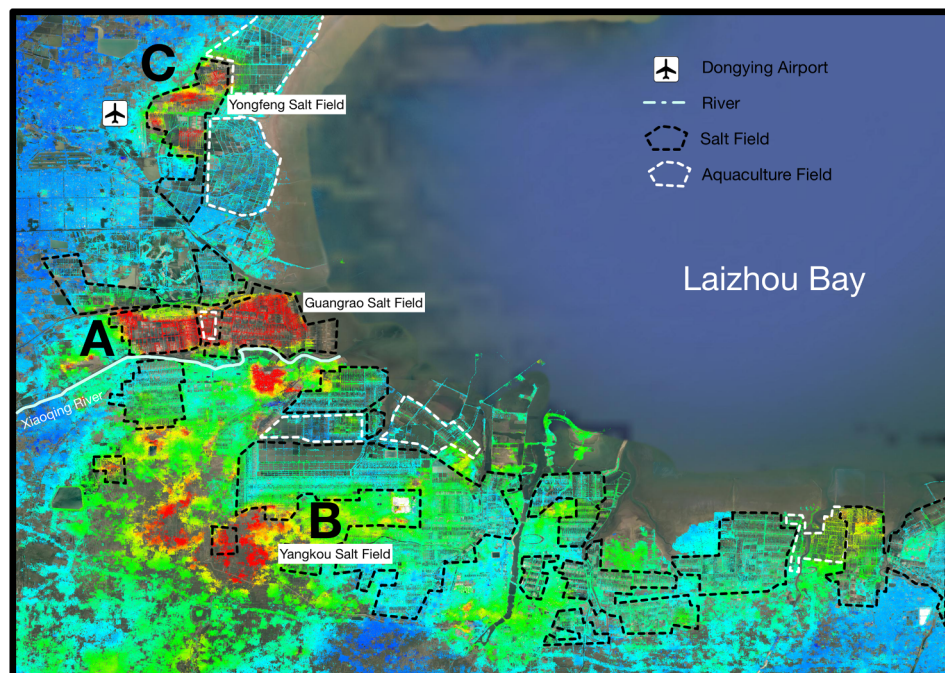


Fig. 11. Vertical subsidence rate map around Laizhou Bay over the period 2015–2018.

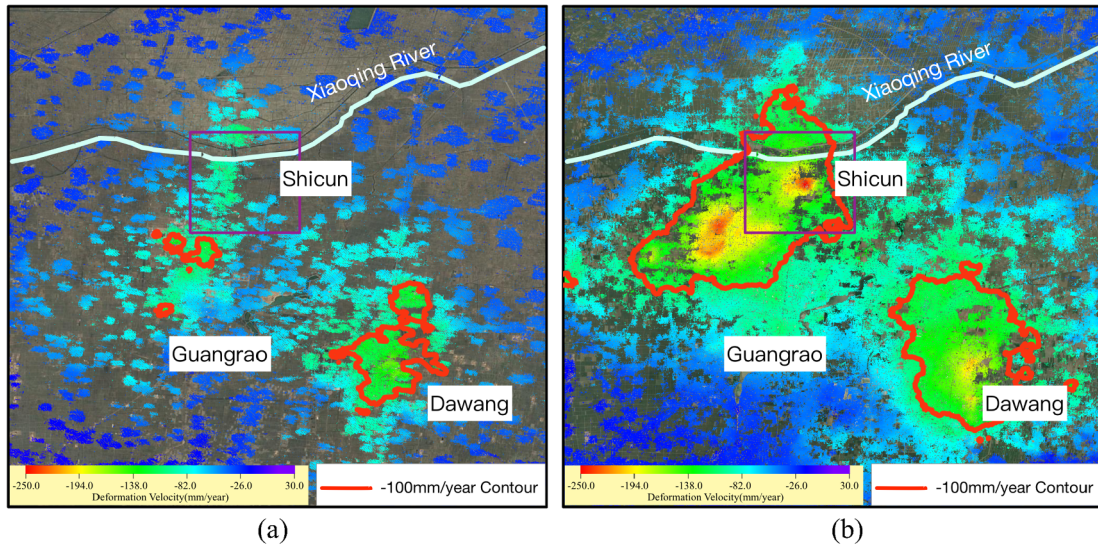


Fig. 13. Vertical subsidence rate map around Guangrao over the periods of (a) 2007–2010 and (b) 2015–2018.



Fig. 14. Optical image around Shicun in 2007, 2011 and 2015, marked with a purple rectangle in **Fig. 13**. (a) Enlarged map of the newly built industrial area. (b) Enlarged map of farmland. (For interpretation of the references to colour in this figure legend, the reader is referred to the web version of this article.)



Fig. 15. Damage found in the industrial area.

ways, such as a more rapid relative sea-level rise, the high possibility of seawater intrusion and flooding and associated diseases. Therefore, long-term monitoring of the YRD and other deltas in the world is urgently needed.

6. Conclusion

In this paper, we developed an improved multitemporal InSAR method to map ground subsidence over the YRD area by exploiting both persistent scatterers (PS) and distributed scatterers (DS). Our method achieves a significant increase in MPs than PSI. In particular, to achieve

fast and robust DS preprocessing for large datasets and large areas, the weighted SHP identification method and CWPL optimal phase reconstruction are utilized.

Our method is applied to ASAR, S-1A and S-1B datasets to obtain a comprehensive and detailed ground subsidence measurement over the YRD during the periods of 2007–2010 and 2015–2018. Cross-sensor comparison of the derived subsidence rates from the S-1A and S-B datasets is conducted to evaluate the accuracy of the derived deformation results. The results derived from the ASAR dataset are further validated using external leveling data. Then, we analyze the spatial-temporal changes of the ground subsidence characteristics over the YRD, and the

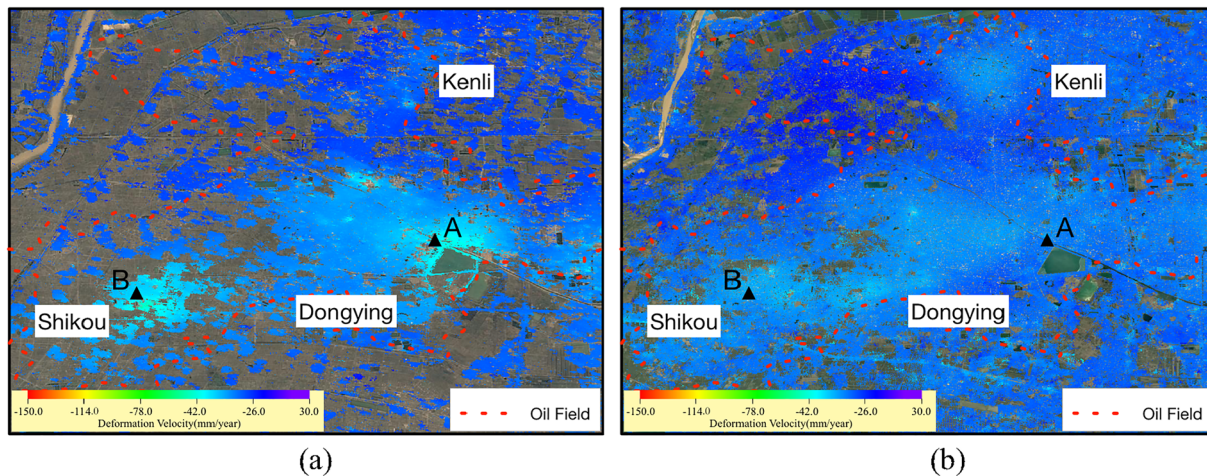


Fig. 16. Vertical subsidence rate map around Dongying over the periods of (a) 2007–2010 and (b) 2015–2018.

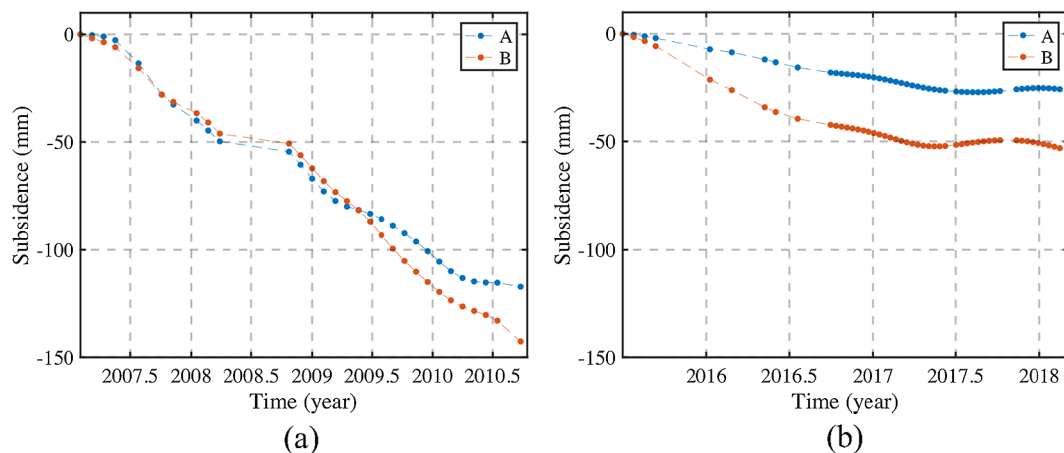


Fig. 17. Accumulated subsidence at points A and B, as marked in Fig. 16, over the periods of (a) 2007–2010 and (b) 2015–2018.

possible causal factors of the subsidence are analyzed. Specifically, the major findings obtained through this research are as follows:

First, our method reveals remarkably comprehensive and detailed ground subsidence fields over the YRD, with an increase in MPs of 15 and 5 times for the ASAR and S-1 datasets, respectively, compared with the Tomo-PSInSAR method.

Second, the cross-track comparison of the derived surface vertical deformation rates using S-1A and S-1B datasets shows a 9.85 mm/yr standard deviation of the difference, which indicates that the derived ground subsidence results over the YRD are reliable. Moreover, compared with the leveling measurements, the accuracy of derived surface deformation rate maps from the ASAR dataset reaches 4.58 mm/yr. This suggests that the proposed algorithm can be utilized as a supplemental tool to the traditional geomeasurement tools to perform precise surface deformation information extraction.

Third, we found that the ground subsidence in the period 2015–2018 shows significant differences from that in the period of 2007–2010. The most obvious change is that several new severe subsidence depressions appear near the coast and show a fast subsidence trend with the maximum deformation rate exceeding 432 mm/yr. In addition, the ground subsidence near Guangrao has become more pronounced. The ground subsidence in the old oil extraction region of Dongying-Kenli-Shikou shows a slowing trend.

Fourth, owing to the high spatial density of the MPs based on the proposed method, we observe that the newly built, linear, manmade facilities, such as the Dezhou-Dajiawa railway, opened to traffic in September 2015, and the Jinan-Dongying highway, opened to traffic in

December 2016, have caused local ground subsidence along their lengths in the YRD.

Finally, the possible causes of ground subsidence over the YRD are analyzed in detail. Overextraction of underground brine for salt production is identified as the primary causal factor for the ground subsidence near the coastal area of the YRD. Moreover, ground subsidence caused by groundwater exploitation for industries, agriculture and fishery aquaculture, oil exploitation and excessive pressure on the surface by manmade structures are also detected over the YRD.

Taking the YRD as an example, we illustrate the potential of our method for detailed and comprehensive ground subsidence measurements over large areas. Moreover, our method can easily be extended to other ground deformation monitoring applications in natural regions, such as landslides, permafrost, volcanoes, etc. However, we are still faced with the dilemma of reprocessing all the data when new data become available. The integration of newly acquired data into past deformation detection results is the next step for our research.

Acknowledgements

This work was supported by the National Key Research and Development Program of China under Grant 2017YFB0502700 and the Open Fund of Key Laboratory of Urban Land Resources Monitoring and Simulation, Ministry of Land and Resources (KF-2016-02-025). The authors would like to thank the European Space Agency for providing the Envisat ASAR and Sentinel-1 data. We also thank the anonymous reviewers for their comments and corrections.

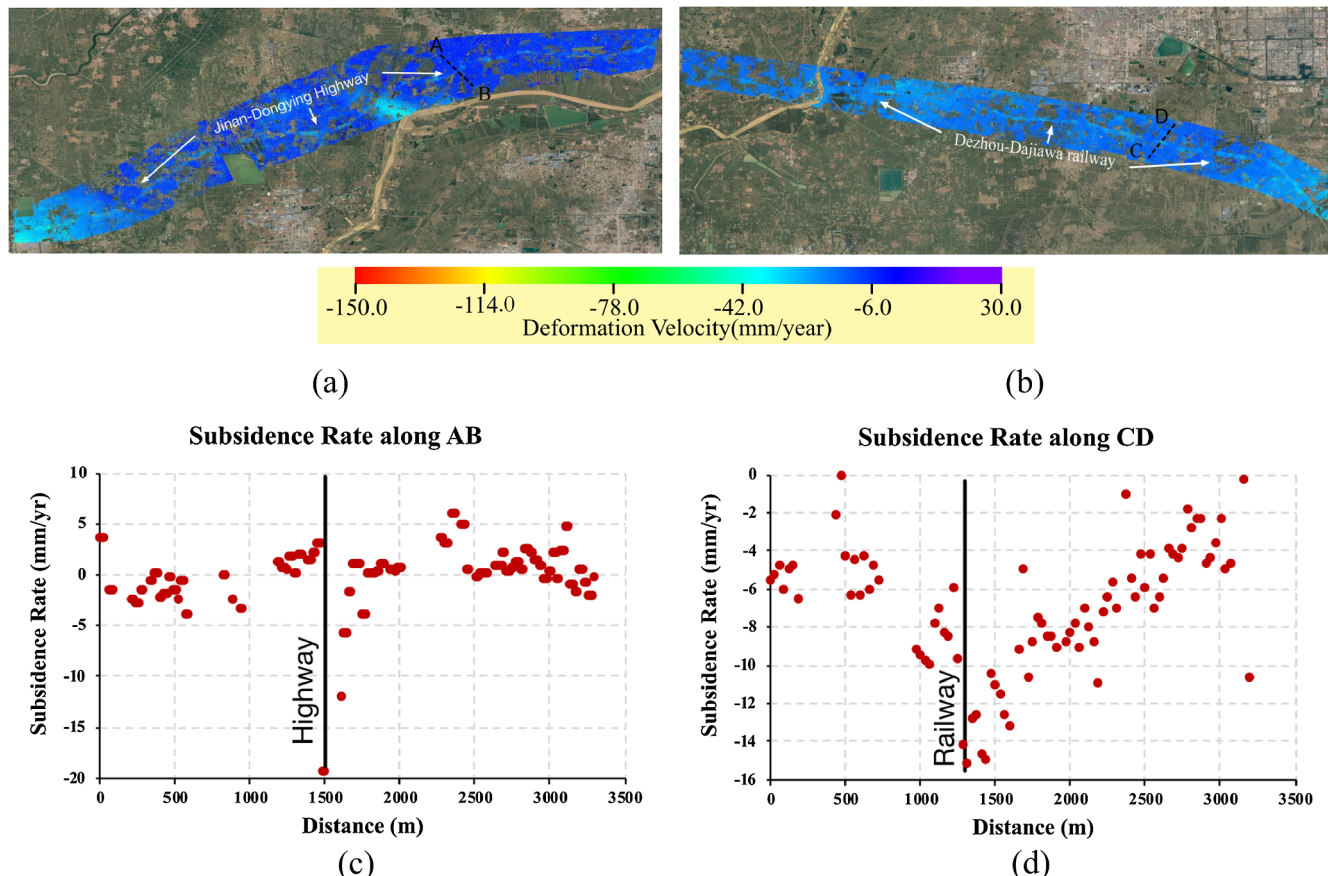


Fig. 18. The vertical subsidence rate map along (a) Jinan-Dongying highway and (b) Dezhou-Dajiawa railway. (c) Subsidence rate profile A-B. (d) Subsidence rate profile C-D.

References

- Bamler, R., Hartl, P., 1998. Synthetic aperture radar interferometry. *Inverse Problems* 14 (4), R1.
- Berardino, P., Fornaro, G., Lanari, R., Sansosti, E., 2002. A new algorithm for surface deformation monitoring based on small baseline differential SAR interferograms. *IEEE Trans. Geosci. Remote Sensing* 40 (11), 2375–2383.
- Bernstein, D.S., 2005. Matrix Mathematics: Theory, Facts, and Formulas with Application to Linear Systems Theory, vol. 41 Princeton University Press, Princeton.
- Cao, N., Lee, H., Jung, H.C., 2015. Mathematical framework for phase-triangulation algorithms in distributed-scatterer interferometry. *IEEE Geosci. Remote Sensing Lett.* 12 (9), 1838–1842.
- Cao, N., Lee, H., Jung, H.C., 2016. A phase-decomposition-based PSInSAR processing method. *IEEE Trans. Geosci. Remote Sensing* 54 (2), 1074–1090.
- Chaussard, E., Amelung, F., Abidin, H., Hong, S.H., 2013. Sinking cities in Indonesia: ALOS PALSAR detects rapid subsidence due to groundwater and gas extraction. *Remote Sensing Environ.* 128, 150–161.
- Chu, Z.X., Sun, X.G., Zhai, S.K., Xu, K.H., 2006. Changing pattern of accretion/erosion of the modern Yellow River (Huanghe) subaerial delta, China: based on remote sensing images. *Mar. Geol.* 227 (1–2), 13–30.
- Crosetto, M., Monserrat, O., Cuevas-González, M., Devanthéry, N., Crippa, B., 2016. Persistent scatterer interferometry: a review. *ISPRS J. Photogramm. Remote Sensing* 115, 78–89.
- Dong, J., Zhang, L., Tang, M., Liao, M., Xu, Q., Gong, J., Ao, M., 2018. Mapping landslide surface displacements with time series SAR interferometry by combining persistent and distributed scatterers: a case study of Jiaju landslide in Danba, China. *Remote Sensing Environ.* 205, 180–198.
- Ferretti, A., Prati, C., Rocca, F., 2001. Permanent scatterers in SAR interferometry. *IEEE Trans. Geosci. Remote Sensing* 39 (1), 8–20.
- Ferretti, A., Fumagalli, A., Novali, F., Prati, C., Rocca, F., Rucci, A., 2011. A new algorithm for processing interferometric data-stacks: SqueeSAR. *IEEE Trans. Geosci. Remote Sensing* 49 (9), 3460–3470.
- Fornaro, G., Verde, S., Reale, D., Paucilullo, A., 2015. CAESAR: An approach based on covariance matrix decomposition to improve multibaseline-multitemporal interferometric SAR processing. *IEEE Trans. Geosci. Remote Sensing* 53 (4), 2050–2065.
- Guarnieri, A.M., Tebaldini, S., 2008. On the exploitation of target statistics for SAR interferometry applications. *IEEE Trans. Geosci. Remote Sensing* 46 (11), 3436–3443.
- Hansen, P.C., O’Leary, D.P., 1993. The use of the L-curve in the regularization of discrete ill-posed problems. *SIAM J. Sci. Comput.* 14 (6), 1487–1503.
- Hooper, A., 2008. A multi-temporal InSAR method incorporating both persistent scatterer and small baseline approaches. *Geophys. Res. Lett.* 35 (16).
- Huber, P.J., 1964. Robust estimation of a location parameter. *Ann. Math. Stat.* 35 (1), 73–101.
- Lanari, R., Mora Sacristán, Ó., Manunta, M., Mallorquí Franquet, J.J., Berardino, P., Sansoti, E., 2004. A small baseline DInSAR approach for investigating deformations on full resolution SAR interferograms. *IEEE Trans. Geosci. Remote Sensing* 42 (7), 1377–1386.
- Liu, Y., Huang, H.J., 2013. Characterization and mechanism of regional land subsidence in the Yellow River Delta, China. *Nat. Hazards* 68 (2), 687–709.
- Liu, Y., Huang, H., Liu, Y., Bi, H., 2016. Linking land subsidence over the Yellow River delta, China, to hydrocarbon exploitation using multi-temporal InSAR. *Nat. Hazards* 84 (1), 271–291.
- Liu, P., Li, Q., Li, Z., Hoey, T., Liu, Y., Wang, C., 2015. Land subsidence over oilfields in the Yellow River Delta. *Remote Sensing* 7 (2), 1540–1564.
- Liu, D.C., Nocedal, J., 1989. On the limited memory BFGS method for large scale optimization. *Math. Program.* 45 (1–3), 503–528.
- Ma, P., Lin, H., 2016. Robust detection of single and double persistent scatterers in urban built environments. *IEEE Trans. Geosci. Remote Sensing* 54 (4), 2124–2139.
- Nicholls, R.J., Cazenave, A., 2010. Sea-level rise and its impact on coastal zones. *Science* 328 (5985), 1517–1520.
- Shi, C., Zhang, D., 2003. Processes and mechanisms of dynamic channel adjustment to delta progradation: the case of the mouth channel of the Yellow River, China. *Earth Surf. Process. Landforms: J. British Geomorphol. Res. Group* 28 (6), 609–624.
- Shi, C.X., Zhang, D., You, L.Y., Li, B.Y., Zhang, O.Y., 2007. Land subsidence as a result of sediment consolidation in the Yellow River Delta. *J. Coastal Res.* 173–181.
- Syvitski, J.P., Kettner, A.J., Overeem, I., Hutton, E.W., Hannon, M.T., Brakenridge, G.R., Day, J., Vrsmarty, C., Saito, Y., Giosan, L., Nicholls, R.J., 2009. Sinking deltas due to human activities. *Nat. Geosci.* 2 (10), 681–686.
- Törnqvist, T.E., Wallace, D.J., Storms, J.E., Wallinga, J., Van Dam, R.L., Blaauw, M., Derkse, M.S., Klerks, C.J., Meijneken, C., Snijders, E.M., 2008. Mississippi Delta subsidence primarily caused by compaction of Holocene strata. *Nat. Geosci.* 1 (3), 173–176.
- Yagüe-Martínez, N., Prats-Iraola, P., Gonzalez, F.R., Brcic, R., Shau, R., Geudtner, D., Eineder, M., Bamler, R., 2016. Interferometric processing of Sentinel-1 TOPS data. *IEEE Trans. Geosci. Remote Sensing* 54 (4), 2220–2234.
- Zebker, H.A., Villasenor, J., 1992. Decorrelation in interferometric radar echoes. *IEEE Trans. Geosci. Remote Sensing* 30 (5), 950–959.
- Zhang, L., Ding, X., Lu, Z., 2011. Ground settlement monitoring based on temporally coherent points between two SAR acquisitions. *ISPRS J. Photogramm. Remote Sensing* 66 (5), 489–500.

- Sensing 66 (1), 146–152.
- Zhang, Y., Huang, H., Liu, Y., Liu, Y., Bi, H., 2018. Spatial and temporal variations in subsidence due to the natural consolidation and compaction of sediment in the yellow river delta, china. Mar. Georesour. Geotechnol. 1–12.
- Zhang, S., Wang, Y., Shi, D., Xu, H., Pang, X., Li, M., 2004. Fault-fracture mesh petroleum plays in the Jiyang Superdepression of the Bohai Bay Basin, eastern China. Mar. Petrol. Geol. 21 (6), 651–668.
- Zhu, X.X., Bamler, R., 2010. Very high resolution spaceborne SAR tomography in urban environment. Geosci. Remote Sens., IEEE Trans. 48 (12), 4296–4308.
- Zhu, X.X., Bamler, R., 2011. Let's do the time warp: multicomponent nonlinear motion estimation in differential SAR tomography. Geosci. Remote Sens. Lett., IEEE 8 (4), 735–739.